ENTRAINMENT OF AIR DRIVEN BY ROTATIONAL FIELD INSIDE VISCOUS LIQUIDS

Prajapati M.[1], Kumar P.[1,*], Das A.K.[1] and Mitra S.K.[2]
[1]Department of Mechanical and Industrial Engineering,
Indian Institute of Technology Roorkee, 247667, India,
[2]Lassonde School of Engineering,
York University, Toronto,
Ontario M3J 1P3, Canada,
E-mail: parmod.12347@gmail.com

ABSTRACT

Here, we propose an intelligent method for entrainment of air inside viscous liquids using submerged rotational mechanisms. A cylindrical disc is immersed inside liquid with its axis transverse to the nominal interfacial plane and rotated at wide range of rotational Reynolds number (4.88 - 14.64). This configuration is simulated using grid based volume of fluid technique in air-polybutene pair. A dip in nominal interface profile is observed at low disc rotations however, gradual progress of rotational inertia has resulted in elongation of interface in the form of a filament of air progressing inside liquid. Transient progress of entrainment depicts pointed curvature like cusped singularities in its profile during the early stages. When this cusp like entrainment gets into the high inertial zone, it grows in radial direction, along with its downward growth due to the centrifugal effect of the surrounding liquid. The interplay of inertia and viscous resistance is also controlled by the initial submergence of the rotating disc along with its rotational inertia. The outcome of the present study could be utilized for the design of chemical reactors, mixing processes and devices relating transfer process as working principle.

INTRODUCTION

Entrainment of air inside liquid is a common occurrence in many daily life situations and industrial applications [1-4], such as pouring of liquid, applying paints or preventive coatings to surfaces, etc. The inclusion of air is sometimes beneficial, for example enhancement in rate of chemical reactions. However, it can be unfavourable for many industrial situations too creating intrusions [5]. Amidst other impact related methods for origination of entrainment, application of rotational inertia has become popular as it can create steady intrusion of gas in liquid [6-9]. It destabilizes the free surface and initiates entrainment in the form of thin and lengthy filaments [9]. The earliest work in this field is reported by Tharmalingam and Wilkinson [1] where they confirm the formation of liquid film around the rotating cylinder periphery which is partially submerged inside liquid. They also measured the thickness of wrapped liquid film at different angles along cylinder periphery measured in the direction of cylinder rotation using capacitance probe. A theoretical formulation has also been employed to predict the variation of liquid film and validate experimental observations. The theoretical predictions are based on the analogy of flat surface obliquely withdrawn from liquid. This idea of solid surface coating due to its rotation is further progressed by Bolton and Middleman [2] towards the entrainment of air inside liquid from its immersing end. The speed at which entrainment initiates is referred to as critical speed and is expressed in terms of Capillary number $\left(Ca = \frac{\mu r \omega}{\sigma}\right)$for Newtonian liquids. They have articulated the viscous and inertia dominant zones based on the cylinder rotations which act against the surface tension to produce cusp (a line singularity of curvature) like entrainment inside the liquid pool.

NOMENCLATURE

a	[m]	Thickness of the disc
Ca	[-]	Capillary number derived using radius of roll as length scale
$\boldsymbol{D}$	[s^{-1}]	Deformation tensor
f_b	[kg/m^{2}s^2]	Body force per unit volume
H	[m]	Distance between the nominal interface location and top surface of the disc
$\boldsymbol{n}$	[-]	Vector normal to the interface
P	[Pa]	Pressure
r	[m]	Radius of disc
Re	[-]	Rotational Reynolds number based on the radius of disc as length scale
$\boldsymbol{u}$	[m/s]	Velocity vector
x	[m]	Cartesian axis direction
y	[m]	Cartesian axis direction
Special characters		
ρ	[kg/m^3]	Density of fluid
σ	[N/m]	Surface tension between gas-liquid pair
ω	[s^{-1}]	Angular velocity of disc rotations
μ	[kg/ms]	Dynamic viscosity of fluid
∂	[-]	Partial derivative
$\boldsymbol{\nabla}$	[m^{-1}]	Del operator
τ	[N/m^2]	Shear stress
λ	[m^{-1}]	Mean curvature of the interface between gas and liquid pair
δ_s	[-]	Kronecker delta operator whose value is 1 at interface only
Subscripts		
l		Liquid phase
g		Gaseous phase

Velocity profiles of the coated liquid film are reported by Campanella and Cerro [3] at wide range of immersion angles for viscous liquids. The velocity profiles of the enveloped liquid film are plotted as function of angular position along cylinder periphery. The perturbation of stratified interface between liquid-liquid layers is demonstrated by Joseph et al. [4] for different liquid-liquid pairs. They observed coating of thin sheet of low viscous liquid on a steady rotating cylinder and articulated that low viscous liquids move in the zone of high shear, to act as a lubricant in order to minimize the torque (dissipation). A fingering instability of cusp like water film has also been observed by them for silicon oil and water combination over an aluminum rod where cusp has continuously generated the water droplets to form an emulsion of water volumes in silicon oil. Interfacial interactions using horizontally located cylinders are also shown by Joseph et al. [6], Jeong and Moffatt [7] and Joseph [8] towards the formation two dimensional cusped interfaces (a line singularity of curvature) in the convergent zone between the counter rotating cylinders. Joseph et al. [6] expressed the critical rotational speed of the cylinder for cusp formation in terms of non-dimensional parameter Capillary number for both Newtonian and non-Newtonian liquids. Jeong and Moffatt [7] have further progressed in their analytical formulation using vortex dipole concept to analyze cusp like interfacial singularities. They have also employed qualitative experimental measurements using air and polybutene by completely submerging cylinders inside liquid pool. With an intelligent description of previous studies, Joseph [8] discussed the important features of cusp formation and doubted whether it is an apparent cusp or sharp interfacial instability/true cusp. Moreover all these studies [6-8] considered the symmetrical cylinder rotations, however, the influence of asymmetric rotational field is described in a recent effort by Kumar et al. [9] taking both cylinder rotation based and diametric asymmetry into consideration. They have shown entrainment of air inside viscous liquid in the form of lengthy filaments as an aftermath of cusp caused by viscous pumping. Similar entrainment profiles are shown by Eggers [5] in case of liquid jet impingement on the liquid pool. Kumar et al. [9] have also shown the bending of entrained filaments towards the cylinder of higher inertia. They concluded that diametric rotational asymmetry enhances the rate of entrainment in comparison to its counterpart of cylinder rotation based asymmetric field at same average rotational Reynolds numbers. In all these studies [6-9] the axis of rotating elements are kept parallel to the nominal interface. However, a recent study [10] has shown the entrainment of oil by translating a circular disc inside water starting from nominal interface. They have located the disc in such a manner so that its axis is transverse to the interface and employed constant velocity motors to translate the disk inside water. In present effort, we have placed the disk inside the liquid pool below the interface and it is rotated at wide range of rotational speeds to initiate entrainment of gas from the interface. We obtained entrainment profiles starting from the steady cusp, towards the formation of thin lengthy gas filaments which split into bubbles once these come inside the inertial zone near the surface of the disc.

MODEL DESCRIPTION

Numerical simulations of gas entrainment inside liquid pool are performed using Eulerian approach based volume of fluid framework. Multilevel quad tree [11] based open source Gerris solver [12] has been used to simulate the phenomenon. A schematic representation of simulation domain is given in Figure 1 which comprises of a cylindrical disc having 20 mm radius placed in vertical orientation with its top surface at H submergence below the interface. Polybutene (ρ = 910 kg/m^3, μ = 3.90 kg/ms and σ = 0.034 N/m) is used as the viscous liquid with air as the lighter phase. Rotational Reynolds number $Re = \frac{\rho \omega r^2}{\mu}$ of the disc is used as the measure of its inertia and its value is varied from 4.88 to 14.64.

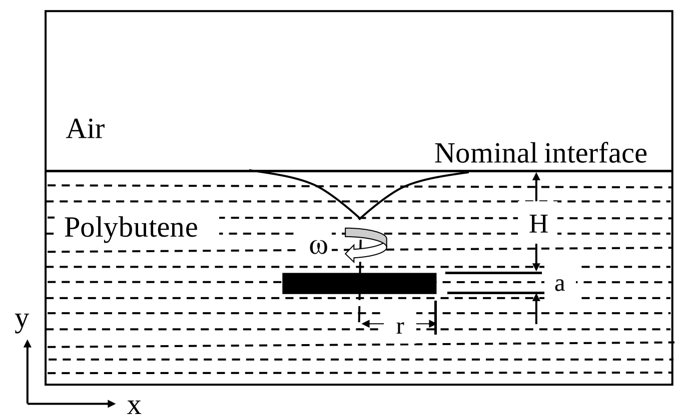

Figure 1 Schematic representation of simulation domain

Discretization of continuity and momentum equations (1-2) for transient, incompressible flow with variable density and surface tension is employed to carry forward the numerical procedure.

$$\nabla . \boldsymbol{u} = 0, \tag{1}$$

$$\rho \left(\frac{\partial \boldsymbol{u}}{\partial t} + \boldsymbol{u} \cdot \nabla \boldsymbol{u} \right) = -\nabla p + \nabla . \boldsymbol{\tau} + \sigma \lambda \delta_s \boldsymbol{n} + f_b . \tag{2}$$

In equations (2) stress tensor $\boldsymbol{\tau}$ can be described as $\boldsymbol{\tau} = 2\mu \boldsymbol{D} = \mu \left(\frac{\partial u_j}{\partial x_i} + \frac{\partial u_i}{\partial x_j} \right)$. In case of two phase flow with immiscible fluids surface tension is also considered in the momentum equation to account for forces acting on the interface. In expression of surface tension, Dirac delta operator is employed to ensure that surface tension should act at interface only. Last term has been incorporated in the momentum equation to account for the body forces which is gravitational acceleration in the present study. Volume of fluid method solves only one momentum equation for both the phases. Therefore volume fraction (α) of liquid phase is employed [12] to express cell averaged flow density and viscosity as:

$$\rho = \alpha \rho_l + (1 - \alpha) \rho_g , \tag{3}$$

$$\mu = \alpha\mu_l + (1-\alpha)\mu_g. \tag{4}$$

Volume fraction of a cell changes with the propagation of interface. Hence, the temporal evolution of volume fraction is updated using advection equation (5), as given here:

$$\frac{\partial\alpha}{\partial t} + \nabla\cdot(\alpha\boldsymbol{u}) = 0. \tag{5}$$

Cells with non integral volume fraction occupy the interface (presence of both liquid as well as gaseous phase). Time-splitting projection method [13] is employed with staggered in time discretization [12] of volume fraction and pressure to provide second order accurate time discretization and results in following system of discretized equations (6-9):

$$\rho_{n+\frac{1}{2}}\left[\frac{\boldsymbol{u}_* - \boldsymbol{u}_n}{\Delta t} + \boldsymbol{u}_{n+\frac{1}{2}}\cdot\nabla\boldsymbol{u}_{n+\frac{1}{2}}\right] = \nabla\cdot\left[\mu_{n+\frac{1}{2}}(\boldsymbol{D}_n + \boldsymbol{D}_*)\right] + (\sigma\lambda\delta_s\boldsymbol{n})_{n+\frac{1}{2}}, \tag{6}$$

$$\frac{\alpha_{n+\frac{1}{2}} - \alpha_{n-\frac{1}{2}}}{\Delta t} + \nabla\cdot(\alpha_n\boldsymbol{u}_n) = 0, \tag{7}$$

$$\boldsymbol{u}_{n+1} = \boldsymbol{u}_* - \frac{\Delta t}{\rho_{n+\frac{1}{2}}}\nabla p_{n+\frac{1}{2}}, \tag{8}$$

$$\nabla\cdot\boldsymbol{u}_{n+1} = 0. \tag{9}$$

Information of $\boldsymbol{u}_*$ obtained from equation (6) is employed to update pressure using Poisson like equation as:

$$\nabla\cdot\left[\frac{\Delta t}{\rho_{n+\frac{1}{2}}}\nabla p_{n+\frac{1}{2}}\right] = \nabla\cdot\boldsymbol{u}_*. \tag{10}$$

Second order accurate, unconditionally stable Crank-Nicholson scheme is used for discretization of viscous term and velocity advection term is estimated using second order Bell-Colella-Glaz upwind scheme [14]. This scheme is conditionally stable for CFL number smaller than one. Piecewise-linear interface capturing [12] has been used to solve advection equation (7) for the volume fraction. System of discretized equations (6-9) is solved on the platform of multilevel Poisson solver Gerris [12].

Adaptation of the mesh has been done based on the gradient of volume fraction as shown in Figure 2(a). Figure 2(a) clearly shows the fine cells near the interface and meshes are coarsened in the zone away from the interface. The phenomenon of entrainment is simulated at five different minimum cell sizes to achieve the grid independence. The depth of entrainment inside the liquid pool from its nominal position is plotted as function of time for rotational Reynolds number of 9.76. Entrainment penetration rate has shown the shown closeness between the values obtained for minimum grid size of 97.66 and 48.83 μm as shown in inset of Figure2(b). The qualitative comparison of entrainment profiles near the surface of the disc is also shown in inset of Figure 2(b). We obtained minimum mesh size of 97.66 μm as grid independent solution.

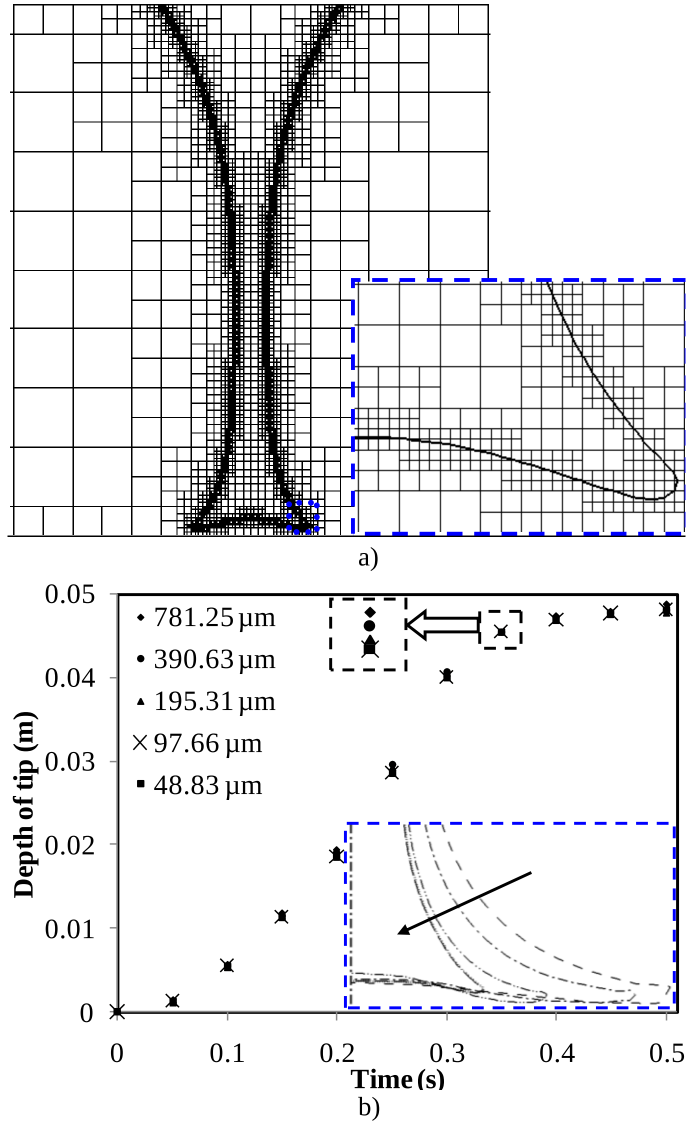

Figure 2 a) Mesh details near the interface and b) variation of entrainment for five different minimum cell sizes at rotational Reynolds number of 9.76. Mesh size decreases in the inset figure showing interface profiles in the direction of arrow

RESULTS AND DISCUSSIONS

We observed that at very low disc rotations interface has remained almost unchanged. However, gradual progress of the rotational inertia results in formation of downward facing dip near the axis of symmetry. This situation is shown in Figure 3(a) for rotational Reynolds number of 4.88. An intuitive observation of Figure 3(a) clearly depicts the cusp like interfacial structure (in the inset) at the line of symmetry. Further progress of the disc rotations led to the deep entrainment of gaseous phase inside liquid pool in the form lengthy filaments. This situation is shown in Figure 3(b) for rotational Reynolds number of 9.76. Subsequent evolution of the interface for such situations results in development of small gas bubbles inside the deep liquid. These gas bubbles tend to move away from the disc surface due to the centrifugal inertia of the surrounding medium.

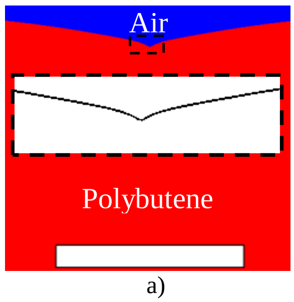

Figure 3 Transformation from steady cuspoidal profile to formation of lengthy gas filament, a) Re = 4.88 and b) Re = 9.76

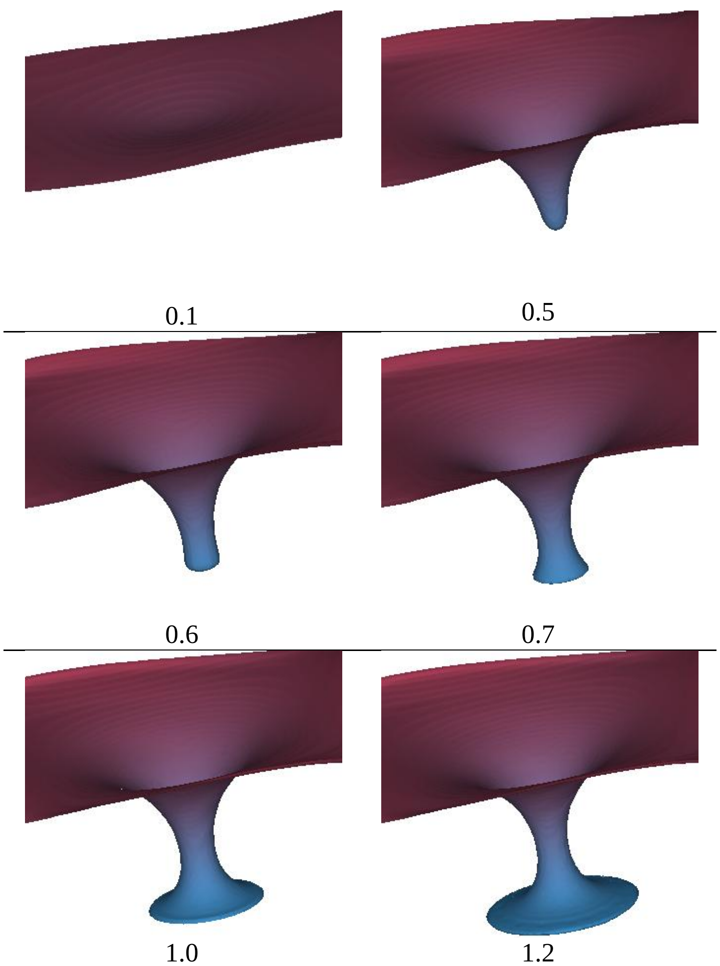

Figure 4 Temporal evolution of the entrainment profile at rotational Reynolds number of 9.76. Time values given here are in seconds

In order to have more insights of the physical phenomenon, temporal evolution of the three dimensional interfacial profile is shown in Figure 4 for rotational Reynolds number of 9.76. The nominal interface profile is flat between the two phases, whereas the initiation of entrainment due to disc rotations can be observed from Figure 4 at time equals to 0.1 s. Entrainment initiates in the form of a wide circular dip whose deepest portion is pulled by the inertia of the disc. This inertial pull has led to the elongation of the interface in downward direction near the axis of symmetry, as shown in Figure 4 for time equals to 0.5 s. Further progress of the interface has resulted in growth of its tip in radial direction (at time equals to 0.6 s in Figure 4). This radial growth of the entrained profile becomes more prominent as during its traversal inside liquid pool (from time equals 0.6 to 0.7 s of Figure 4). Entrainment profile takes the shape of the bell as it reaches near the top surface of the disc and widens from the bottom due to strong centrifugal inertia (at time equal to 1.0 and 1.2 s of Figure 4). In addition the periphery of the bottom most section of the entrainment profile is governed by the strength of rotational inertia of the disc. Detailed elaboration on effect of disc rotations on entrainment patterns is given in the subsequent subsection.

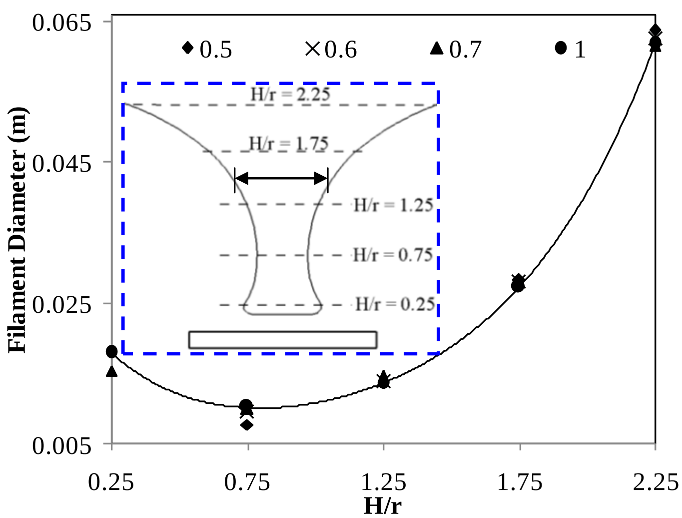

Figure 5 Temporal evolution of the entrainment profile at rotational Reynolds number of 9.76. Time values given here are in seconds

In addition to the penetration of entrainment inside liquid pool, measurement of its span at different locations along the axis of the disc is also a parameter of utmost importance. Efforts have been made to plot the diameter of the entrained filament as function of its vertical locations measured from the top surface of the disc (Figure 5). The location of any arbitrary plane is non-dimensionalized with the radius of the disc. Inset of Figure 5 shows the different locations at which measurement of the gaseous film diameter are taken. Diameter of entrainment profile decreases as it moves towards the disc surface and reaches a minimum value (Figure 5). After getting minima the entrainment starts growing in radial direction as it reaches inside the periphery of rotational inertia. The span of entrainment remains almost constant for all the time steps before its minima. However, entrainment profile grows with time in radial direction as it reaches near the disc surface (H/r ~

0). This can be seen from Figure 5 on moving from 0.7 s to 1 s at H/r = 0.25.

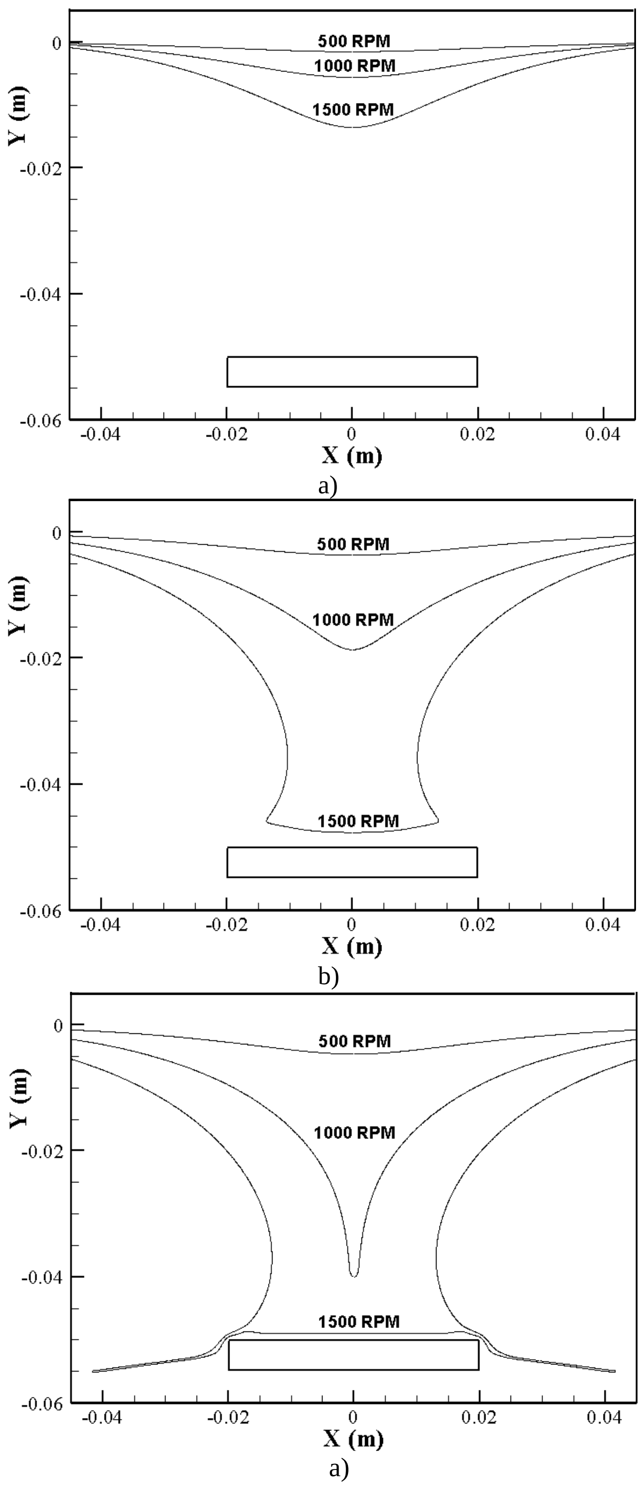

Figure 6 Comparison of entrainment profiles for three different disc rotations at a) 0.1 s, b) 0.2 s and 0.3 s

Effect of Rotational Inertia

The control of entrainment rate and its profile is extremely important as it governs the many industrial processes. Therefore, we have made the efforts to study the influence of disc inertia on the entrainment rates and its profile inside the liquid pool. Figure 6 shows the entrainment profiles superimposed on the same plot for three different disc rotations at equal time levels. It can be observed from this figure that entrainment penetrates at slower rates in case of lower disc rotations. However, an entrained filament enhances their rate of traversal when it comes closer to the disc surface. Efforts have also been made to quantify the entrainment rates in terms of its penetration below the nominal interfacial location. The penetration of entrainment tip at the axis of symmetry is plotted as function time for wide range of rotational inertia in Figure 7. Figure 7 depicts that entrainment rate is infinitely small for rotational inertia of 4.88 after the formation of initial dimple. Increase of rotational Reynolds number from 4.88 to 5.86 has resulted in significant improvements in the entrainment and it is able to reach till the top surface of the disc. However, the entrainment rate is not same during its complete journey. Further progress of the disc rotations has resulted faster acceleration of the entrainment rates with smaller initial delay. Sufficiently higher rotational inertia (Re = 14.66) has shown growth of entrainment at almost same rate throughout its complete traversal.

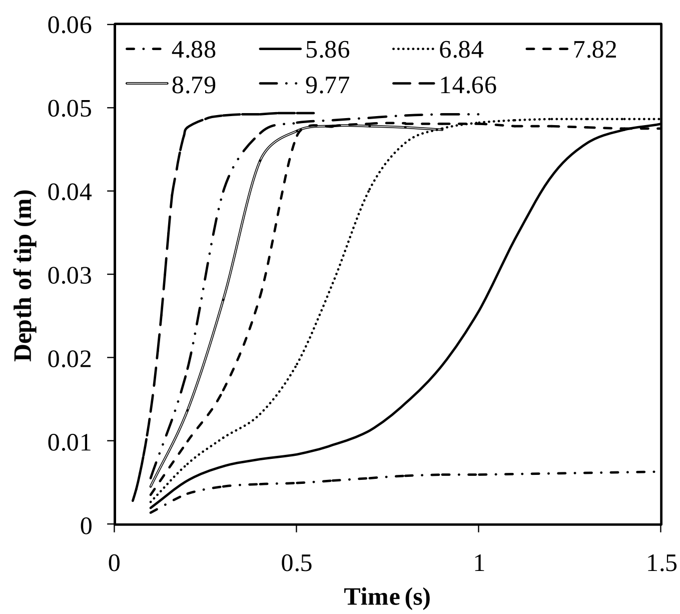

Figure 7 Variation of entrainment rate for different rotational inertial fields. Here, values quoted in legend are the rotational Reynolds number taking disc radius as the length scale

Effect of Nominal Interface Location

After establishing the effect of the disc rotations, it is also of paramount interest to study the influence of nominal interface height on the entrainment patterns at fixed rotational inertia. To evaluate this, we have varied the H/r ratio from 2.5 to 5.5 for a constant Reynolds number of 14.64. The steady interface profiles for these three cases are shown in Figure 8(a). It clear from the Figure 8(a) that disc rotation is not sufficient to produce the entrainment for H/r = 5.5. However, decrease of H/r from 5.5 to 4.0 has resulted in very thin and slender entrainment profile. Subsequent decay in nominal interface location has resulted in radial growth of entrainment profile. The quantification of entrainment rates is shown in Figure 8(b) for all these situations. Figure 8(b) reveals that entrainment rates decrease upon increase of nominal interface location from the surface of the disc.

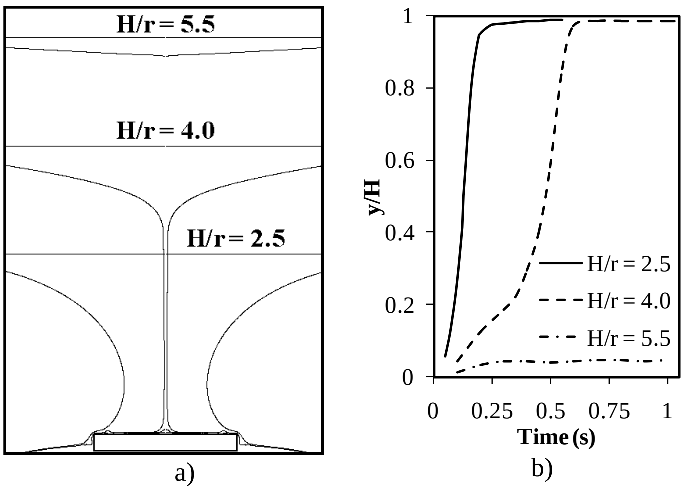

Figure 8 Effect of nominal interface height for Re = 14.64: a) comparison of entrainment profiles and b) measure of entrainment rates

CONCLUSION

Proposals have been made to produce the steady entrainment profiles in the form lengthy gas filaments inside viscous liquid using rotational mechanisms. Evidences of such entrainment profiles are shown using grid based volume of fluid framework for wide range of disc rotations (Re = 4.88-14.64). We observed almost no entrainment situations which transforms to cuspoidal interface profiles upon gradual increase of inertial field. Increase of disc inertia above Re = 4.88 has resulted in entrainment in the form of gas filaments for H/r = 2.5. The nature of the entrainment profile is strongly governed by the rotational inertia of the disc (Re) and its submergence below the nominal interface (characterized by H/r). Increase of H/r ratio above a critical value results in no entrainment situation, however, small H/r ratios leads to the thicker entrained gas filaments. Moderate values of H/r ratio gives very thin and lengthy gas filaments. Entrainment grows with sharp tip during the initial portion of its traversal whereas it grows in radial direction as well as axial direction when it reaches near the disc in the zone of significant rotational inertia.

REFERENCES

[1] Tharmalingam S. and Wilkinson W. L., The coating of Newtonian liquids onto a rotating roll, *Chemical Engineering Science*, Vol. 33, 1978, pp. 1481–1487

[2] Bolton B. and Middleman S., Air entrainment in a roll coating system, Chemical Engineering Science, Vol. 35, 1980, pp. 597–601

[3] Campanella O. H. and Cerro R. L., Viscous flow on the outside of a horizontal rotating cylinder: The roll coating regime with a single fluid, *Chemical Engineering Science*, Vol. 39(10), 1984, pp. 1443–1449

[4] Joseph D. D., Nguyen K., and Beavers G. S., Non-uniqueness and stability of the configuration of flow of immiscible fluids with different viscosities, *Journal of Fluid Mechanics*, Vol. 141, 1984, pp. 319–345

[5] Eggers J., Air Entrainment through Free-Surface Cusps, *Physical Review Letters*, Vol. 86(19), 2001, pp. 4290-4293

[6] Joseph D. D., Nelson J., Renardy M., and Renardy Y., Two-dimensional cusped interfaces, *Journal Fluid Mechanics*, Vol. 223, 1991, pp. 383–409

[7] Jeong J. and Moffatt H. K., Free-surface cusp associated with flow at low Reynolds number, *Journal Fluid Mechanics*, Vol. 241, 1992, pp. 1–22

[8] Joseph D. D., Understanding cusped interfaces, *Journal of Non-Newtonian Fluid Mechanics*, Vol. 44, 1992, pp. 127–148

[9] Kumar P., Das A. K., and Mitra S. K., Bending and growth of entrained air filament under converging and asymmetric rotational fields, *Physics of Fluids*, Vol. 29, 2017, pp. 022101

[10] Peters I. R., Madonia M., Lohse D. and van der Meer D., Volume entrained in the wake of a disc intruding into an oil-water interface, *Physical Review Fluids*, Vol. 1(3), 2016, pp. 033901

[11] Popinet S., Gerris: A tree-based adaptive solver for the incompressible Euler equations in complex geometries, *Journal Computational Physics*, Vol. 190(2), 2003, pp. 572–600

[12] Popinet S., An accurate adaptive solver for surface-tension-driven interfacial flows, *Journal of Computational Physics*, Vol. 228(16), 2009, pp. 5838–5866

[13] Chorin A., On the convergence of discrete approximations to the Navier-Stokes equations, *Mathematics of Computation Journal*, Vol. 23(106), 1969, pp. 341–353

[14] Bell, J., Colella, P., and Glaz, H., A second-order projection method for the incompressible Navier-Stokes equations, *Journal of Computational Physics*, Vol. 85, 1989, pp. 257–283